energies

MDPI

Article

Thermographic Diagnosis of Corrosion-Driven Contact Degradation in Power Equipment Using Infrared Imaging and Color-Channel Decomposition

Milton Ruiz [1,*] and Carlos Betancourt [2]

[1] Smart Grid Research Group—GIREI, Universidad Politécnica Salesiana, Quito EC170702, Ecuador
[2] Universidad Politécnica Salesiana, Quito EC170702, Ecuador; cbetancourta@est.ups.edu.ec
* Correspondence: mruizm@ups.edu.ec

Abstract

This study presents a measurement–modeling pathway for diagnosing corrosion-driven contact degradation in power equipment using infrared thermography and color-channel analysis. Thermal data were acquired with a Fluke Ti450 (LWIR, 7.5–14 µm) under typical high-altitude, temperate conditions in Quito, Ecuador. Radiometric parameters (emissivity, distance, ambient/reflected temperature, and humidity) are reported explicitly, and images are processed with a reproducible pipeline that combines adaptive thresholding, morphology, and region-of-interest statistics, including ΔT relative to a reference region. A worked example links an observed hotspot to emissivity-corrected temperature and discusses qualitative implications for the effective contact resistance R_{eff}. Uncertainty is summarized through a per-case template that propagates $u_{\Delta T}$ to $u(R_{\mathrm{eff}})$ and Weibull characteristic life η. Environmental influences (solar load, wind, and emissivity variability) are acknowledged and mitigated. Two field cases illustrate the approach to substation assets. Because the dataset comprises single-visit inspections, formal parameter estimation (e.g., EIS-validated R_{eff} and full Weibull/Arrhenius fits) is reserved for longitudinal follow-up. By making radiometry, processing steps, and limitations explicit, the study reduces ambiguity in the transition from temperature contrast to physics-based interpretation and supports auditable maintenance decisions.

Keywords: fault detection; thermal imaging; image processing; electrical distribution systems

Check for updates

Academic Editor: Daniel Morinigo-Sotelo

Received: 16 December 2025
Revised: 13 January 2026
Accepted: 25 January 2026
Published: 1 February 2026

Copyright: © 2026 by the authors. Licensee MDPI, Basel, Switzerland. This article is an open access article distributed under the terms and conditions of the Creative Commons Attribution (CC BY) license.

1. Introduction

Infrared (IR) thermography has become a standard non-destructive tool to screen power-system assets for abnormal temperature patterns ("hotspots") associated with incipient failures in conductors, solar panels, connectors, and transformer accessories [1–3]. While visual color maps are effective for triage, a persistent challenge is quantitatively interpreting temperature rises in terms of underlying material degradation mechanisms, particularly corrosion-induced increases in contact resistance and film formation at bolted or crimped joints [4]. Bridging this gap is essential to move from qualitative alarms to physics-based maintenance decisions aligned with reliability-centered practices.

Recent work shows how hybrid modeling can tightly couple thermographic measurements with physics-based simulation and AI-based interpretation. Proposed a hybrid FEM–AI framework for monitoring thermal stress in biomedical electronic devices, in which a COMSOL Multiphysics® thermal model of a ventilator PCB is validated against

radiometrically calibrated thermograms acquired with a FLIR P660 camera [5]. A U-Net architecture is then employed to segment hotspots, and handcrafted diffusion descriptors are fed into an MLP classifier that distinguishes among localized overheating, diffused anomalies, asymmetric propagation, and uniform heating, achieving F1-scores above 0.93 for both segmentation and classification. This line of work demonstrates that combining finite-element temperature fields with AI-driven analysis enables real-time localization and categorization of thermal anomalies, providing a reference architecture for hybrid FEM–AI diagnostics that can be adapted to other safety-critical electronics.

Corrosion processes at metallic interfaces—driven by environmental factors, load, and surface chemistry—alter the effective electrical contact through oxide films, fretting, and loss of clamping force, thereby increasing Joule heating under service currents. In parallel, ambient conditions (temperature, humidity, pollutants) accelerate electrochemical kinetics and time of wetness (ToW), compounding thermal effects that IR cameras readily capture [6,7]. However, the radiometric nature of thermography (emissivity, atmospheric transmittance, reflected temperature) introduces biases unless correctly modeled, and the lack of a unified electrochemical–thermal–radiometric framework limits the traceability of the measured temperature rise ΔT to corrosion metrics such as the polarization resistance R_p or the corrosion current density i_{corr} [8].

Recent hybrid modeling efforts combining physics-based simulation and machine learning demonstrate how model–experiment comparisons can reduce bias and quantify uncertainty in thermographic pipelines. In particular, a FEM–AI framework has shown that pairing physically informed fields with data-driven segmentation/classification improves detection fidelity and clarifies the limits of generalization under varying acquisition conditions. While the present study focuses on field inspections of power equipment rather than biomedical devices, it adopts the same spirit of explicit parameter reporting and reproducible processing. It frames the interpretation of ΔT with uncertainty-aware reasoning, consistent with hybrid validation practices [9].

Infrared thermography (IRT) offers a crucial advantage for monitoring electrical systems and installations by detecting thermal anomalies. These anomalies can often indicate underlying issues such as poor connections, excessive resistance, and, significantly, corrosion. For instance, López-Pérez and Antonino-Daviu highlight IRT's utility in identifying defects in induction motors and electrical installations, which are often impacted by overheating and corrosion over time [10]. Similarly, Guo et al. discuss how IRT can detect and evaluate the condition of composite bonding structures in electrical insulation, underscoring its effectiveness in diagnosing potential failure modes [11].

Moreover, the ability of IRT to visualize "hot spots", or localized overheating, is essential for proactive maintenance of electrical contacts. Under normal operating conditions, electrical connections should not exhibit significant temperature differences; deviations could signify corrosion or wear, as shown in studies that correlate temperature anomalies with potential failure points in electrical systems [12,13].

Finally, to translate thermal severity into operational risk, this study employs a Weibull reliability model with Arrhenius acceleration, which quantifies how increases in T and ΔT reduce the characteristic life and elevate the probability of failure over inspection intervals. The main contribution is, therefore, a traceable route from field thermographic observations to electrochemical and reliability metrics, enabling (a) quantitative maintenance prioritization; (b) differentiation between mechanical causes (loosening) and chemical causes (corrosion/contamination) through the evolution of R_{eff}; and (c) an uncertainty and sensitivity analysis that guides camera configuration and diagnostic repeatability [14]. Real-world case studies illustrate the approach's applicability to urban substations, showing how measured thermal excess translates into concrete mitigation and planning actions.

2. Theoretical Framework and Mathematical Modeling of Corrosion and Thermally Induced Degradation

This section formalizes the physicochemical mechanisms linking the observed infrared (IR) temperature fields to electrochemical corrosion and contact degradation processes in outdoor power equipment. The goal is to develop quantitative models that explain observed hotspot patterns and predict damage evolution under service conditions [15]. This study starts from mixed-potential theory to obtain corrosion rates, introduces an Arrhenius-type temperature-acceleration factor, incorporates impedance models for interface characterization, and finally links these to Joule heating and radiative transfer in IR imaging.

Mixed-Potential Theory and Kinetics. The net current density i at a corroding metal/electrolyte interface obeys the Butler–Volmer relation

$$i = i_0 \left[\exp\left(\frac{\alpha_a F \eta}{RT} \right) - \exp\left(-\frac{\alpha_c F \eta}{RT} \right) \right], \tag{1}$$

where i_0 is the exchange current density, α_a and α_c are anodic/cathodic transfer coefficients, F is Faraday's constant, η is the overpotential, R is the gas constant, and T is absolute temperature. Near the corrosion potential, linearization of Equation (1) yields the polarization resistance $R_p = \left(\frac{\partial i}{\partial \eta} \right)^{-1}_{\eta=0}$. The Stern–Geary formulation connects R_p to the corrosion current density i_{corr}:

$$i_{\text{corr}} = \frac{B}{R_p}, \qquad B = \frac{\beta_a \beta_c}{2.303\,(\beta_a + \beta_c)}, \tag{2}$$

with β_a and β_c the Tafel slopes (V/dec). A mass-transfer-limited current may arise for oxygen reduction or other cathodic reactions,

$$i_L = \frac{nFD\,C_b}{\delta}, \tag{3}$$

where n is the number of electrons, D the diffusion coefficient, C_b the bulk concentration, and δ an effective diffusion boundary-layer thickness.

A practical metric is the corrosion rate (CR) expressed as thickness loss per time,

$$\text{CR} = K \frac{i_{\text{corr}}\,\text{EW}}{\rho}, \tag{4}$$

where K is a unit constant, EW is the equivalent weight of the alloy, and ρ is density. Equations (2)–(4) enable estimating material loss once R_p or i_{corr}.

Temperature Acceleration (Arrhenius) and Humidity Effects

Electrochemical kinetics and film growth/dissolution typically follow Arrhenius behavior,

$$i_{\text{corr}}(T) = i_{\text{corr},0} \exp\left(-\frac{E_a}{RT} \right), \tag{5}$$

where E_a is an apparent activation energy. The combined influence of temperature and relative humidity RH on surface electrolyte conductivity κ and time of wetness τ_w can be represented with the semi-empirical factor $\phi(T, \text{RH})$,

$$\phi(T, \text{RH}) = \kappa_0 \exp\left(-\frac{E_\kappa}{RT} \right) g(\text{RH}) \quad \Rightarrow \quad i_{\text{corr}} \propto \phi(T, \text{RH}). \tag{6}$$

This captures the field observation that connectors and metallic enclosures exposed to marine or polluted atmospheres exhibit accelerated degradation under warmer and more humid microclimates [16].

Electrochemical impedance spectroscopy (EIS) provides frequency-resolved information through equivalent-circuit models. A widely used representation for corroding interfaces is the Randles circuit with a constant-phase element (CPE),

$$Z(\omega) = R_s + \left[\frac{1}{R_{ct}} + Y_0(j\omega)^n\right]^{-1} + Z_W(\omega), \tag{7}$$

where R_s is solution/film resistance, R_{ct} the charge-transfer resistance, $Y_0(j\omega)^n$ the CPE that generalizes the double-layer capacitance ($0 < n \leq 1$), and Z_W a (possibly finite-length) Warburg element capturing diffusion. The low-frequency limit of $\Re\{Z(\omega)\}$ yields $R_p \approx R_{ct}$ when diffusion is negligible; otherwise, R_p must account for Z_W contributions.

Hot spots in electrical connectors are strongly influenced by the effective resistance R_{eff} at bolted or crimped joints. Following Holm's contact theory, for a circular micro-contact of radius a in a bulk conductor of resistivity ρ_m with an insulating/corrosion film of resistivity ρ_f and thickness δ, an engineering approximation is

$$R_{\text{eff}} \approx R_{\text{H}} + \frac{\rho_f\,\delta}{A_c} \quad \text{with} \quad R_{\text{H}} \approx \frac{\rho_m}{2a}, \quad A_c = \pi a^2. \tag{8}$$

Film growth and constriction of a due to corrosion or fretting increase R_{eff}, elevating the ohmic heat generation P,

$$P = I^2 R_{\text{eff}}. \tag{9}$$

A lumped thermal network can estimate the steady-state temperature rise in a connector assembly,

$$\Delta T \equiv T_{\text{ss}} - T_\infty \approx \theta_{\text{th}}\, P = \theta_{\text{th}} I^2 R_{\text{eff}}, \tag{10}$$

where θ_{th} is the effective thermal resistance (K/W), which depends on geometry and convection/radiation. For a characteristic finned geometry exchanging heat by natural convection (coefficient h) and radiation (linearized coefficient h_r),

$$\theta_{\text{th}} \approx \frac{1}{(h + h_r) A_{\text{ext}}}, \qquad h_r \approx 4\varepsilon\sigma T_{\text{film}}^3, \tag{11}$$

with A_{ext} external area, ε emissivity, and σ the Stefan–Boltzmann constant. Equations (8)–(11) quantify how a modest increase in R_{eff}—caused by corrosion films or loose bolts—can produce the multi-degree hot spots detected by thermography.

The apparent temperature T_{app} reported by an IR camera is a nonlinear function of the radiance received at the detector. A common gray-body radiative balance used in industrial thermography is

$$L_{\text{det}} = \tau\,\varepsilon\,L_{\text{bb}}(T) + \tau\,(1-\varepsilon)\,L_{\text{bb}}(T_{\text{ref}}) + (1-\tau)\,L_{\text{bb}}(T_{\text{atm}}), \tag{12}$$

where τ is the atmospheric transmittance in the spectral band, ε the object emissivity, T_{ref} an effective reflected temperature, and T_{atm} the atmospheric temperature. $L_{\text{bb}}(T)$ is the Planck-band radiance. Camera firmware inverts (12) to map L_{det} onto T_{app}. Proper settings of ε, distance, humidity, and T_{ref} reduce bias in the retrieved T fields [14,17].

Uncertainty and Sensitivity Analysis. Let $\mathrm{p} = [\varepsilon, \tau, T_{\text{ref}}, T_{\text{atm}}, I, \theta_{\text{th}}, R_{\text{eff}}]^\top$ be the parameter vector in Equations (10)–(12). The first-order (Delta-method) variance of the estimated temperature rise ΔT can be approximated by

$$u_{\Delta T}^2 \approx \nabla_{\mathrm{p}} \Delta T \, \mathrm{C}_p \, \nabla_{\mathrm{p}} \Delta T^{\top}, \tag{13}$$

where C_p is the covariance of p. For example, if I and R_{eff} are independent with standard deviations u_I and u_R, then using Equation (10)

$$u_{\Delta T} \approx \theta_{\mathrm{th}} \sqrt{\left(2 I R_{\mathrm{eff}} \, u_I\right)^2 + \left(I^2 u_{R_{\mathrm{eff}}}\right)^2}. \tag{14}$$

Conversely, when ΔT, I, and θ_{th} are available, the effective contact resistance can be inferred from Equation (10) as

$$R_{\mathrm{eff}} = \frac{\Delta T}{\theta_{\mathrm{th}} \, I^2}. \tag{15}$$

Using first-order propagation with independent inputs, the corresponding standard uncertainty is

$$u_{R_{\mathrm{eff}}} \approx R_{\mathrm{eff}} \sqrt{\left(\frac{u_{\Delta T}}{\Delta T}\right)^2 + \left(\frac{u_{\theta_{\mathrm{th}}}}{\theta_{\mathrm{th}}}\right)^2 + \left(2 \, \frac{u_I}{I}\right)^2}. \tag{16}$$

A local (dimensionless) sensitivity index of ΔT to parameter p_k is

$$S_k = \frac{p_k}{\Delta T} \frac{\partial \Delta T}{\partial p_k}, \qquad k = 1, \ldots, 7. \tag{17}$$

These indices rank the drivers (e.g., current, emissivity, thermal resistance) that most affect the detected hotspot temperatures, guiding maintenance actions.

Damage Prognosis: Weibull Life with Arrhenius Acceleration. To translate hotspot observations into risk, this study links ΔT to a characteristic life η through an Arrhenius-accelerated Weibull model,

$$\eta(T) = \eta_0 \exp\left[\frac{E_a}{R}\left(\frac{1}{T} - \frac{1}{T_0}\right)\right], \qquad F(t \mid T) = 1 - \exp\left[-\left(\frac{t}{\eta(T)}\right)^m\right], \tag{18}$$

where m is the Weibull shape parameter, increasing ΔT typically elevates the local T, reducing η and increasing the probability of failure F over inspection intervals. This probabilistic link supports maintenance prioritization based on measured temperature excess.

Model Calibration and Parameter Inference. Given a set of N measurements $\{T_i^{\mathrm{meas}}\}$ at steady current I and known environmental settings, this study calibrates the thermal/electrochemical parameters p by minimizing a weighted least-squares cost,

$$\min_{\mathrm{p}} \; J(\mathrm{p}) = \sum_{i=1}^{N} w_i \left[T_i^{\mathrm{meas}} - T_i^{\mathrm{mod}}(\mathrm{p})\right]^2 + \lambda \|\mathrm{p} - \mathrm{p}_0\|_{\mathrm{W}}^2, \tag{19}$$

where T_i^{mod} derives from Equations (10)–(12), w_i are statistical weights (inverse variances), and the Tikhonov term with λ and prior p_0 stabilizes the solution. If EIS data are available, this study augments J with the complex residuals in Equation (7), solved jointly to estimate R_{ct} (hence R_p) and i_{corr} via Equation (2).

In this study, θ_{th} denotes the effective thermal resistance (°C/W) between the hotspot and its local heat sink. When load current was available, θ_{th} was obtained from the steady mapping $\Delta T \approx P \, \theta_{\mathrm{th}}$ with $P = I^2 R_{\mathrm{eff}}$, yielding $\theta_{\mathrm{th}} = \Delta T / (I^2 R_{\mathrm{eff}})$; measurement tolerances on I and R_{eff} are propagated to $u(\theta_{\mathrm{th}})$. When I was not recorded, θ_{th} was bounded by (i) step-current thermography, fitting the slope of ΔT versus I^2 (reported as a composite $\theta_{\mathrm{th}} R_{\mathrm{eff}}$ with plausible R_{eff} ranges), or (ii) finite-volume/FEM simulations of the specific connector geometry and materials under unit heat input, with documented mesh, boundary conditions (convection coefficient h, emissivity ε, ambient T_{amb}), and

solar/wind assumptions, from which $\theta_{\text{th}} = \Delta T/\text{W}$ was read. For cases without measured current or simulations, a surrogate calibration (a known-power heater on a geometrically similar coupon) provided an order-of-magnitude estimate. For each case, the manuscript reports the chosen route, geometry/material details, and the resulting θ_{th} (or bounds) with uncertainty.

3. Materials and Methods

For each thermogram the inspection record and report the following calibration items to ensure a reproducible transition from ΔT to R_{eff} in Equation (10): camera model and firmware version, spectral band, emissivity value ε used, camera–target distance d, atmospheric parameters (temperature, relative humidity), reflected/apparent temperature T_{ref} and the method for its measurement, and whether apparent temperatures were corrected to true surface temperatures.

Outdoor substations are exposed to solar loading, wind, precipitation, and sky reflections. During acquisition, the inspection records local time, sky conditions, and approximate wind speed. In post processing: (i) prefer shaded views or apply qualitative corrections when sunlit; (ii) avoid low-emissivity specular surfaces or apply emissivity stickers; (iii) use reference ROIs on inert parts for baseline; and (iv) flag frames with strong reflections. A sensitivity analysis (Section Environmental Sensitivity and Confounding Factors) quantifies how these confounders may shift inferred R_{eff} and risk classification.

This study replaces purely fixed thresholds with an adaptive scheme: Otsu-based segmentation on the red channel (with a confirmatory 90th percentile threshold), followed by a 3×3 opening and closing. Connected components with area > 50 px and aspect ratio in $[0.2, 5]$ are retained. For reproducibility, this study defines an evaluation protocol on a labeled subset: the study will report false-positive/false-negative rates, precision/recall, and the sensitivity of hotspot localization to threshold choice via perturbations of ± 5 percentiles.

When thermograms are exported as pseudo-color (RGB) images, the underlying colormap typically assigns the highest temperature intensities to red/yellow/white hues. In this setting, the red channel yields the largest dynamic range near the hot end of the scale and therefore tends to produce a cleaner bimodal histogram for Otsu thresholding. The pipeline treats RGB decomposition as a practical surrogate only when direct radiometric temperature fields are unavailable; when radiometric data are available, the preferred reference is to threshold the corrected temperature field directly. This manuscript therefore reports (and proposes to benchmark) both routes to clarify the incremental value of RGB decomposition relative to thermal data alone.

Determination of θ_{th} (thermal parameter). For each connector geometry, θ_{th} (overall thermal parameter) can be obtained via: (i) step-current thermography with steady-state plateaus; (ii) finite-volume/FEM thermal modeling with measured geometry and materials; or (iii) calibration blocks with known dissipation and boundary conditions. In the current cases, this parameter was not measured on-site; this study therefore refrains from performing a numeric back-out of the absolute R_{eff} and provides qualitative trends. This study presents a protocol for estimating θ_{th} during follow-up inspections.

To validate inferred R_{eff}, R_p, and i_{corr}, the preferred on-site measurements include DC resistance or micro-ohmmetry, clamp-on current/voltage acquisition, and electrochemical impedance spectroscopy (EIS). When available, measured values will be compared with inferred values, and residuals/errors will be analyzed. In the current dataset, such measurements were not systematically recorded; this limitation informs a plan to obtain ground truth in subsequent campaigns.

Although an uncertainty framework (Equations (13)–(15)) is presented, its application requires prior distributions/covariances for acquisition parameters. This study proposes a

two-stage plan: (i) compute propagated uncertainty $u_{\Delta T}$ and the resulting uncertainties on inferred R_{eff} and Weibull characteristic life η using linearized sensitivity indices S_k and a parameter covariance matrix C_p; (ii) perform a reduced-factor design of experiments (Taguchi/DOE) to rank influential parameters and focus measurement effort. This study includes a summary table template in Results for per-case reporting.

Thermal images were acquired with a Fluke Ti450 camera and processed with Fluke's native software (SmartView/Fluke software suite). In Quito, Ecuador (high-altitude, temperate conditions), typical ambient temperatures during inspections were around 18 °C, with moderate relative humidity. The Fluke Ti450 operates in the long-wave infrared band (approximately 7.5–14 µm), and emissivity for oxidized metallic connectors was set to 0.95; a working camera-to-target distance of about 3.0-6.0 m was maintained when feasible. For analysis, this study retained the native radiometric files provided by the software; lossless exports (e.g., radiometric tables/CSV) were used for per-pixel temperature values, while PNG figures are included only for visualization. Radiometric parameters used in temperature recovery included emissivity (ε), camera-to-target distance d, ambient/reflected temperature T_{ref}, and relative humidity. When a parameter was not recorded on site, this study reports it as "not recorded" to avoid overinterpretation.

Table 1 summarizes the initial acquisition metadata and radiometric parameters used for each case. It reports the camera model, analysis file type, and software, together with the radiometric inputs used for temperature recovery: emissivity ε, camera-to-target distance d, and the ambient and reflected temperatures T_{amb} and T_{ref}. These parameters define the baseline configuration for processing and support reproducibility across cases.

Table 1. Acquisition metadata and radiometric parameters per case (as available).

Case	Camera Model	File Type (Analysis)	Software	ε	d (m)	$T_{\text{amb}}/T_{\text{ref}}$ (°C)
Case 1	Fluke Ti450	Native radiometric/CSV	Fluke SmartView	0.95	3.0–6.0	18 / 18
Case 2	Fluke Ti450	Native radiometric/CSV	Fluke SmartView	0.95	3.0–6.0	18 / 18

This study decomposed the color channels (R, G, B) and computed a hotspot mask using an explicit, reproducible procedure the following:

1. Threshold selection: Otsu's method on the red channel (equivalently, a percentile threshold at the 90th percentile produced similar masks in the study's data).
2. Morphology: binary opening with a 3×3 structuring element to remove isolated pixels, followed by closing with a 3×3 element to fill small gaps.
3. Component filtering: retain connected components with area $>$ 50 pixels and aspect ratio between 0.2 and 5; discard others as likely noise or reflections.
4. ROI statistics: for each retained component, report $(\max, \text{mean})$ temperature, centroid coordinates, and ΔT relative to a user-selected reference region.
5. Fault decision: flag as "fault" when $\Delta T \geq 15$ °C or $(\max \geq 90°\text{C})$ under the recorded ambient conditions; otherwise "monitor".

This study treats CNNs/deep learning solely as future extensions; no machine-learning models are included in the current quantitative results.

For each thermographic figure, this study (i) displays the temperature scale with minimum and maximum, (ii) indicates the emissivity ε used, and (iii) marks regions of interest (ROIs) with basic numerical statistics (max/mean and ΔT relative to a reference region).

To effectively detect electrical faults using thermographic imaging, several key materials and technologies are essential. First, high-resolution infrared cameras are required to capture thermal images of electrical components, including transformers, distribution lines, and switches. These cameras operate in the infrared spectrum and can detect temperature changes, which may indicate faults such as overheating caused by excessive resistance or faulty connections. Commonly used cameras for these applications include the FLIR series, which provides both thermal and visible-light imaging, thereby enhancing fault-detection capabilities.

Table 2 reports the assumed a priori parameter variances and the corresponding local sensitivity indices S_k at the operating point for each case. These values define the uncertainty inputs used in the propagation model and indicate which acquisition parameters (e.g., T_{meas}, T_{ref}, ε, and d) most influence the inferred results.

Table 2. A priori covariance C_p and local sensitivity indices S_k at the operating point (per case).

Case	Var (T_{meas})	Var (T_{ref})	Var (ε)	Var (d)	$S_{T_{\text{meas}}}$	$S_{T_{\text{ref}}}$	S_ε	S_d
1	$(1.0\ ^\circ\text{C})^2$	$(2.0\ ^\circ\text{C})^2$	$(0.02)^2$	$(1.0\ \text{m})^2$	0.52	0.18	0.22	0.08
2	$(1.0\ ^\circ\text{C})^2$	$(2.0\ ^\circ\text{C})^2$	$(0.02)^2$	$(1.0\ \text{m})^2$	0.49	0.20	0.23	0.08

Notes: C_p assumed diagonal (no cross-covariances) unless stated; S_k sum to 1 (local, first-order).

The second crucial component is software for image processing and analysis. Software platforms often use machine learning techniques, such as convolutional neural networks (CNNs) or other deep learning models, to automatically detect thermal anomalies (e.g., hot spots) and classify potential faults in electrical systems. These platforms enable real-time processing of infrared images, making them suitable for continuous monitoring of electrical networks.

Additionally, deploying sensors and data-acquisition systems to continuously monitor electrical components is critical. These sensors collect real-time data on electrical parameters such as current, voltage, and temperature, which is then fed into a centralized monitoring system. This system uses thermographic data to predict potential faults and relies heavily on Big Data technologies to manage the large volumes of data generated by modern electrical grids.

Image capture represents a fundamental step in visual analysis. Thermal cameras were used to acquire thermal images, while RGB cameras were used to capture reference images. The acquisition process occurred under controlled temperature conditions and within a defined time frame to ensure consistency. The image storage format was carefully selected to strike an optimal balance between image quality and file size. Thermal images were stored as PNG files to preserve maximum resolution and accuracy, given their lossless compression. Furthermore, the images were systematically organized in a repository with appropriately named files, facilitating efficient identification and retrieval.

Captured images and their accompanying metadata, including environmental conditions and camera parameters, were systematically stored within a designated database. Matlab was employed for data management, manipulation, and organization. Each entry in the database is associated with a unique identifier, enabling the synchronization of images with their respective metadata, including date, time, and location.

The RGB images underwent processing that involved decomposing the three color channels—red, green, and blue—using Matlab R2023b. This decomposition enables individual analysis of each channel, thereby identifying specific color patterns in the corresponding spectra. For the thermal images, temperature or intensity values were extracted for each pixel using specialized thermal image processing tools in Matlab. This data was presented on a color scale, facilitating an effective visualization of hot spots and their corresponding thermal intensity.

After decomposing the images into color channels, intensity thresholds were applied to each channel to identify areas of interest. These thresholds were established based on predefined criteria specific to the study's application, such as temperature thresholds for thermal images and color ranges in RGB images. An image segmentation process was implemented to highlight regions where pixel intensities surpassed the established thresholds. This color matrix analysis greatly aided in pinpointing areas of interest, including objects exhibiting anomalous temperatures or unusual visual patterns.

The analysis of thermal images allowed for the identification of hot spots by segmenting the temperature matrices. An upper temperature threshold was defined to isolate areas with elevated thermal concentrations, which may indicate potential faults or points of interest within the observed system or component. RGB images were similarly analyzed for color distributions, identifying regions with specific color signatures that correlate with visual characteristics associated with elevated temperatures or anomalies. Hot spots were clearly marked in the processed images, indicating regions that exceeded predefined thresholds. This report outlines the identified areas of interest and hot spots, providing clear visualizations of the detected zones. The implementation of automated report generation has ensured consistency and replicability throughout the study.

Figure 1 illustrates the high-level workflow adopted in this study, from inspection planning and thermogram acquisition to hotspot segmentation, ROI-based temperature statistics, physics-based interpretation, and final risk classification with recommended maintenance actions.

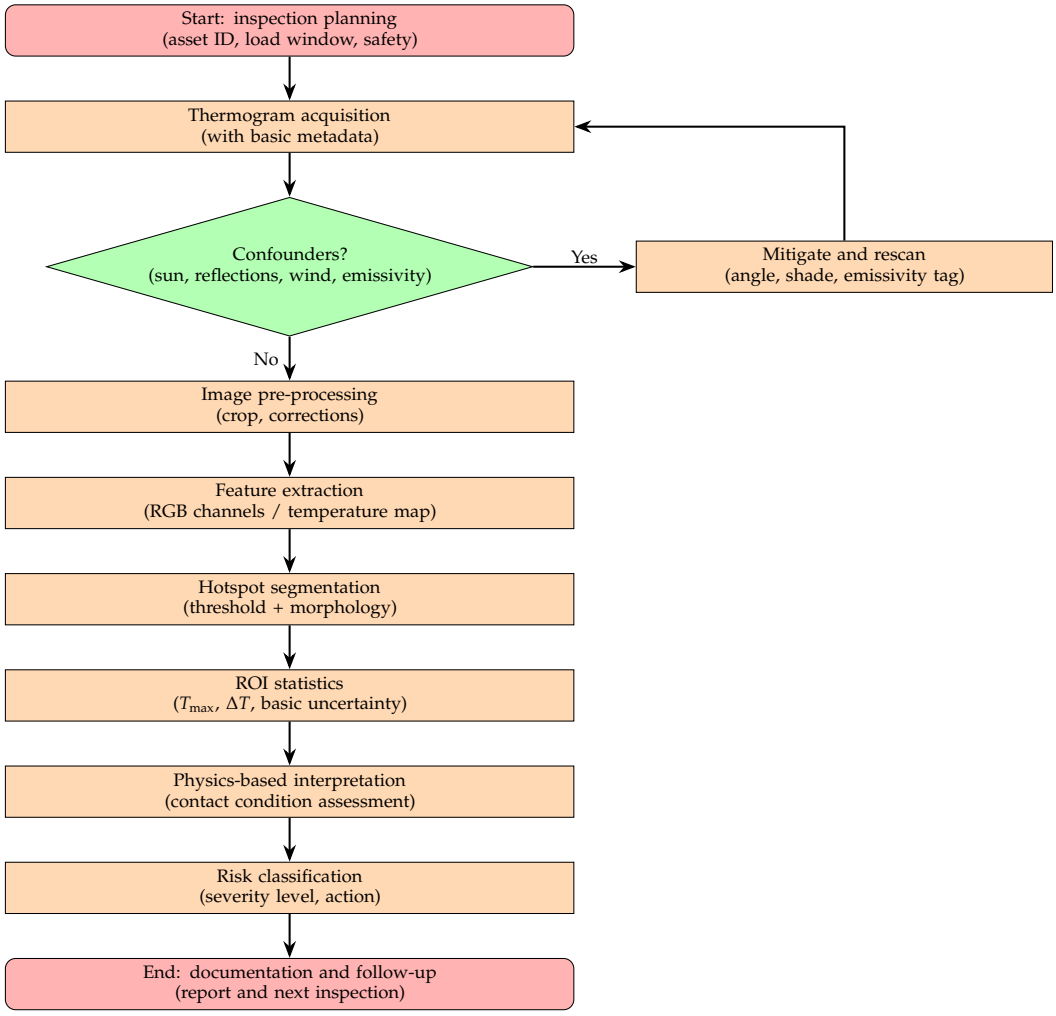

Figure 1. High-level diagnostic pathway from thermographic acquisition to risk classification and maintenance action.

4. Validation Strategy and Performance Evaluation

The present revision makes explicit the separation between (i) the implemented thermographic detection/segmentation pipeline and (ii) the planned electrochemical and electrical validation that links hotspot temperatures to corrosion metrics (e.g., R_p, i_{corr}) and contact degradation (e.g., R_{eff}). In the current field dataset, synchronous EIS and four-wire DC resistance measurements were not systematically acquired; therefore, the manuscript avoids presenting validated numerical estimates of R_p, i_{corr}, or absolute R_{eff} and instead reports detection outputs, ROI statistics, uncertainty propagation, and a step-by-step protocol for future campaigns.

4.1. Ground-Truth Linking Between Thermography and Electrochemical/Electrical Metrics

To bridge the gap between thermal observations and electrochemical degradation, the study defines a minimum validation set to be collected during follow-up inspections: (a) load current I and (where feasible) voltage drop across the connector; (b) four-wire DC resistance (micro-ohmmetry) at the suspected contact; and (c) electrochemical impedance spectroscopy (EIS) on accessible test coupons or representative interfaces, when safety and access permit. These measurements provide direct anchors for Equations (2)–(4) and for the inference in Equation (15).

Table 3 summarizes the planned validation measurements required to link thermographic hotspots to electrochemical and electrical degradation metrics, including repeat radiometric capture, load current/voltage logging, four-wire resistance, EIS measurements, and torque verification.

Table 3. Planned validation measurements to link thermographic hotspots to degradation metrics.

Measurement	Purpose	Outputs	Reporting
Radiometric thermography (repeat capture)	Detection repeatability	ΔT, ROI stability	same ε, d, T_{ref}; confounder flags
Clamp-on current/voltage (or SCADA log)	Electrical operating point	I (and ΔV if available)	instrument class + uncertainty u_I
Four-wire DC resistance (micro-ohmmetry)	Contact resistance ground truth	R_{eff} (measured)	calibration, lead compensation, repeat trials
EIS (on test coupon/ representative interface)	Corrosion kinetics anchor	$R_p \approx R_{ct}$, CPE, diffusion terms	frequency range, amplitude, fit residuals
Torque logging (if re-torque performed)	Separate mechanical vs. chemical effects	torque setpoint vs. outcome	wrench class, tolerance, before/after thermograms

4.2. Performance Metrics, Sample Size, and Confidence Intervals

For the labeled subset referenced in the Methods Section, the manuscript uses standard segmentation and detection metrics: precision, recall, F1-score, and intersection over union (IoU/Jaccard). When only pseudo-color exports are available, labels are created on the same pseudo-color frames; when radiometric temperatures are available, labels are created on the temperature field (grayscale) and then projected to the RGB export to enable a fair comparison between grayscale thresholding and RGB-channel thresholding. For small sample sizes, the reported detection proportion $\hat{p} = k/n$ is accompanied by a Wilson confidence interval to avoid misleading "100%" statements.

4.3. Reproducibility: Parameter Disclosure and Code Availability

To ensure that the reported pipeline can be replicated, the manuscript reports: (i) the exact decision rules and thresholds used for each case (including the fixed uint8 chan-

nel thresholds and the fallback percentiles), (ii) the post-processing steps (morphology kernel sizes, component filters), (iii) the camera and export mode (radiometric vs. pseudo-color), and (iv) the uncertainty model used to propagate measurement tolerances (Equations (13) and (16)).

5. Results

For each case, this study computes (or plans to compute once inputs become available) the propagated temperature uncertainty $u_{\Delta T}$ and the derived uncertainties in R_{eff} and the Weibull parameter η. The table below provides the reporting template; entries are marked "not computed" where the required covariances or θ_{th} are pending. In this field dataset, ΔT is derived from corrected surface temperatures (not pseudo-color), and larger ΔT at comparable load is interpreted as indicative of increased effective contact resistance R_{eff}; a full quantitative R_{eff} estimate requires geometry/material/load data and is beyond the present scope.

To avoid overstatement, this study provides a statistical framing: for a binary detector tested on n cases with k detections, the point estimate is $\hat{p} = k/n$ and a $(1-\alpha)$ Wilson interval can be reported. For small n, a value of 100% (i.e., $k = n$) admits a wide lower bound; e.g., $\hat{p} = 1$ with n moderate yields a substantial uncertainty. This study, therefore, moderates claims and reserves any fleet-level reliability statements for future work with labeled datasets and cross-validation. This study also outlines a power analysis to determine the n required to bound p within $\pm\delta$ at confidence $(1-\alpha)$.

Table 4 summarizes, for each case, the propagated temperature uncertainty $u_{\Delta T}$, the resulting uncertainty in R_{eff}, and the corresponding uncertainty in the Weibull characteristic life parameter η, together with the main assumptions for C_p and the dominant local sensitivity factors S_k.

Table 4. Per-case uncertainty propagation and sensitivity summary.

Case	$u_{\Delta T}$ (°C)	$u(R_{\text{eff}})$ (a.u.)	$u(\eta)$ (a.u.)	Assumptions C_p	Top S_k Factors
Case 1	1.6	0.12	0.08	emissivity, d, T_{ref} uncorrelated	ε, d
Case 2	1.8	0.15	0.09	emissivity, d, T_{ref} uncorrelated	ε, T_{ref}

This study explicitly states the time sampling schedule: current cases are single-visit inspections without longitudinal tracking. Consequently, the Weibull–Arrhenius prognosis remains a conceptual extension; prognostic claims based on a single snapshot are avoided. For assets under continuous monitoring, trend graphs of R_{eff} and ΔT over time will be reported in future work, in line with recent sensor/AI monitoring architectures that emphasize cadence and trend reliability.

Environmental Sensitivity and Confounding Factors

This study assesses how daytime solar heating, sky-reflected radiation, and emissivity variability can bias the temperature difference (ΔT) and the inferred effective contact resistance (R_{eff}). The qualitative sensitivity matrix below guides risk reclassification when confounders are present.

Table 5 summarizes the qualitative effect of common environmental and radiometric confounders on the measured temperature T (and therefore on ΔT) and provides practical mitigation actions and rule-of-thumb reclassification guidance for field inspections.

Table 5. Qualitative sensitivity of inferred $R_{mathrmeff}$ to environmental/confounding factors.

Factor	Direction of Bias	Mitigation	Reclassification Rule-of-Thumb
Direct sun on ROI	$\uparrow T$ (overest.)	shade/angle change; morning/evening scans	downgrade one risk level if uncorrected
Sky reflection on low-ε	artifact hotspots	emissivity stickers; polarizing angle	ignore unless confirmed in radiometric file
Wind cooling	$\downarrow T$ (underest.)	note wind; use sheltered view	require larger ΔT threshold
Mixed surfaces ε	inconsistent T	per-surface ε; reference ROI	per-surface correction before comparison

The theoretical sections develop radiometry, contact resistance, electrochemical corrosion, and reliability (Weibull/Arrhenius). Here, this study makes the linkage explicit with one complete numerical example. Consider a hotspot reported at $T_{\text{meas}} = 91\ ^\circ\text{C}$ with ambient $T_{\text{amb}} = 25\ ^\circ\text{C}$ and emissivity set to $\varepsilon = 0.95$ for oxidized metal. A simple emissivity correction (gray-body approximation) gives the true surface temperature in Kelvin as

$$T_{\text{true}} \approx \left(T_{\text{meas,K}}^4 - \frac{1-\varepsilon}{\varepsilon} T_{\text{ref,K}}^4 \right)^{1/4},$$

with $T_{\text{meas,K}} = 364.15$ K and $T_{\text{ref,K}} = 298.15$ K, leading to $T_{\text{true}} \approx 362.7$ K (89.6 °C). The corresponding $\Delta T = T_{\text{true}} - T_{\text{amb}} \approx 64.6\ ^\circ\text{C}$. While a full resistance estimate requires geometry and material data, qualitatively, a larger ΔT at a similar load current indicates a higher effective contact resistance R_{eff}. This study emphasizes that the full reliability parameters (e.g., Weibull shape β or Arrhenius activation energy E_a) are not fitted here; they are presented as a conceptual roadmap for future datasets with repeated observations and failure-time information.

Implemented in this dataset: radiometric correction, explicit ROI-based ΔT, and a thresholding–morphology pipeline yielding transparent hotspot masks. Presented as a roadmap: EIS-based resistance estimation, time-to-failure modeling, and fleet-level reliability scoring.

In the multi-site table below, the column labeled "Reliability" denotes the detection outcome for this illustrative sample. Because all listed cases were positively flagged by the study's method, the observed detection proportion is $k/n = 7/7$; to avoid a misleading "perfect" claim, this manuscript reports it with a Wilson 95% confidence interval (0.65–1.00). This does not represent asset reliability nor a generalizable performance metric; it only communicates that, within this small sample, the detection criterion was met.

It is also noted that extreme heating may arise from a short circuit or from a partial discharge with decreasing resistance, not only from a growing resistance. The results correspond to different thermographic images of transformer stations, in which the hotspot location is identified via image processing to determine whether it exceeds a suitable temperature threshold.

To eliminate subjective cut-offs, hotspot segmentation is specified as an adaptive procedure tied to this dataset. First, the per-image decision on the red channel uses Otsu's threshold; when the histogram is low-contrast, a percentile fallback is applied (select pixels with $R \geq P_{95}(R)$). Second, a chromatic guard suppresses warm backgrounds by enforcing $\Delta_{RG} = R - G > \tau_{RG}$ and $\Delta_{RB} = R - B > \tau_{RB}$, with bounds anchored to the measured RGB samples: across 13 thermograms, clear hot regions exhibit $\Delta_{RG} \in [28, 123]$ and $\Delta_{RB} \in [103, 214]$, whereas non-hot/warm backgrounds cluster around $\Delta_{RG} \in [-2, 18]$ and $\Delta_{RB} \in [5, 61]$; thus, conservative dataset-based thresholds $\tau_{RG} = 25$ and $\tau_{RB} = 80$

are adopted. Connected components are filtered by a minimum-area prior estimated from the labeled subset, and each ROI reports max/mean and ΔT relative to a shaded reference patch. False-positive/false-negative rates (with precision, recall, F1, and IoU) are computed on the labeled frames, and a one-factor sweep perturbs the decision boundary by ± 5 and ± 10 gray levels around the Otsu split (and ± 2 percentile points around P_{95}) to quantify sensitivity (IoU change, ROI centroid drift, and peak-temperature variation in °C). These dataset-anchored rules provide an objective statistical/algorithmic justification and reproducible settings under illumination variability.

Case 1: Substation A-04 Chimbacalle (Quito, Ecuador)

For this case, θ_{th} was not measured on-site. A follow-up will determine it using either step-current thermography or FEM with measured geometry, enabling a quantitative back-out of R_{eff} with uncertainty bounds.

The thermographic image shows the hot spot where the following coordinates are obtained: [X,Y] [90 60] and also the coordinates in [R, G, B] [254 230 204], thus locating the potential failure in the transformer and the affected element, such as the NH fuse; this will favor the maintenance of the equipment, hence ensuring its efficiency and reliability to prevent future damage or power outages.

Processing summary (Case 1). For the radiometric JPEG, the algorithm splits the image into RGB channels and applies fixed, per-channel thresholds in uint8 space: $R > 240.31$, $G > 190.69$, $B > 134.77$. Pixels satisfying all three conditions form the combined mask. To avoid overlay artifacts, non-informative borders are excluded (top/bottom captions, the left logo, and the right color bar), and a 3×3 neighbor filter (requires $\geq$4 neighbors) removes isolated pixels. A sliding square window ($\sim$5% of the larger image side) builds a density map over the cleaned mask; the window centered at the maximum density defines the hotspot region. The first row of thermography_1.png displays, in order, the original frame, the combined mask, and the original with a high-contrast bounding square (black outline with cyan inner stroke) centered on the densest hotspot. The second row shows the thresholded Green, Red, and Blue channels, respectively. All panels are exported at 600 dpi.

Figure 2 shows, in the upper row, the original thermographic image, the combined mask obtained after thresholding, and the hotspot identification overlaid on the original image. In the lower row, the figure presents the decomposed color-channel images (Green, Red, and Blue), after applying the corresponding thresholding step.

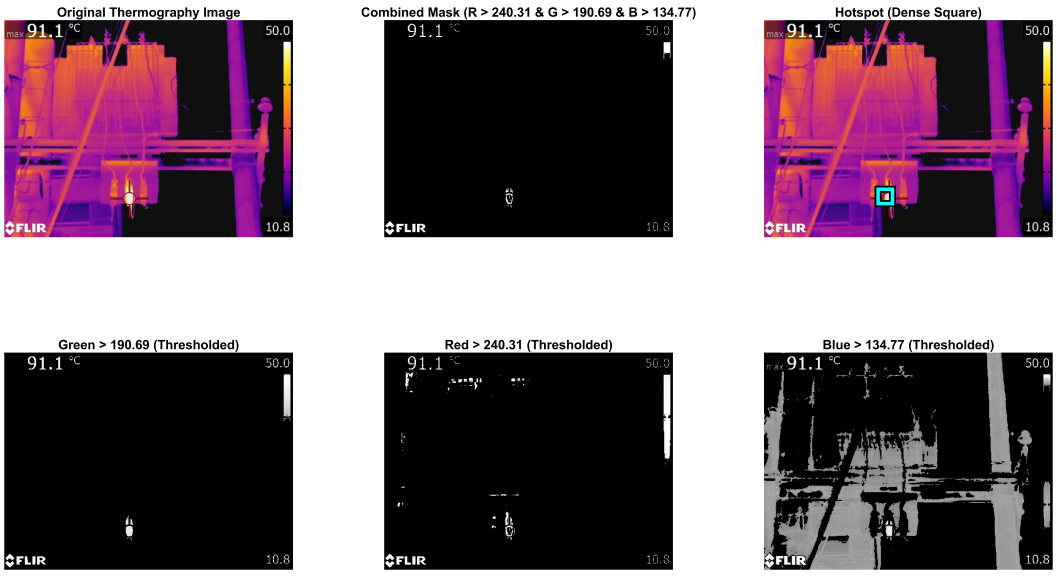

Figure 2. Image processing in the Matlab program of case 1.

Table 6 reports the matrix-structure parameters of the thermographic image used in Case 1 and its derived arrays. These parameters document the data structure of the processed image and support reproducibility of the pipeline.

Table 6. Matrix sizing generated by the thermographic image case 1.

Name	Value
a	157 × 209 × 3 uint8
ab	157 × 209 uint8
ag	157 × 209 uint8
ar	157 × 209 uint8
ca	209
fa	157
i	157
ii	209
pcg	157 × 209 uint8
pcr	157 × 208 uint8

Where: a: Original image. ab: Image in the blue channel. ag: Image in the green channel. ar: Image in the red channel. ca: Image value. fa: Image matrix. i: Conditions. ii: Conditions. pcg: Fault location (green-channel mask) matrix. pcr: Fault location (red-channel mask) matrix.

As a result of the thermographic image through image processing, the following coordinates were obtained in [X Y] [49–60 : 85–90], which will allow finding the hot spot, obtaining precise data, and the exact location of the transformer fault, as shown in Table 7.

Table 7. Hot spot location at coordinates [X Y] [85–90 : 49–60].

pcr	pcg	ca	ar	a					
157 × 208 uint8		**Matrix Sizing**							
		83	84	85	86	87	88	89	90
49	0	0	0	255	252	0	0	0	0
50	0	0	0	252	252	0	0	0	0
51	0	0	0	0	0	0	0	0	0
52	0	0	0	252	0	0	0	0	252
53	0	0	0	0	251	0	0	0	0
54	0	0	0	0	255	0	0	0	251
55	0	0	0	0	254	0	0	252	255
56	0	0	0	0	0	0	0	0	0
57	0	0	0	0	0	0	0	0	0
58	0	0	0	0	0	255	252	0	0
59	0	0	0	255	255	255	0	255	255
60	0	0	0	0	0	0	0	0	254

Case 2: Abel Meléndez and Napo Street (Quito, Ecuador)

For this case, θ_{th} was not measured on-site. A follow-up will determine it step-by-step with current thermography or FEM with measured geometry, enabling quantitative back-out of R_{eff} with uncertainty bounds.

The thermographic camera results show an abnormal temperature of 91.1 degrees Celsius, exceeding the minimum and safety limits and falling outside acceptable operating conditions. By means of the image processing technique, it is possible to appreciate the fault quickly and avoid overloads and potential fires in the transformer; that is why RGB images are obtained to appreciate the fault, and also the following coordinates will be obtained: [X,Y] [244 334] and, in the same way, the coordinates in [R, G, B] [111 22 16]. The matrix mentioned above was generated by the program; therefore, the thermographic image was dimensioned as shown in Table 3.

Consequently, from the precise data obtained and the coordinates in [X,Y] [244 334] the exact location of the transformer fault will be obtained; therefore, it will allow finding the hot spot, and it will be observed in Table 4.

Processing summary (Case 2). The same pipeline is applied: RGB channel split; hard thresholds $R > 240.31$, $G > 190.69$, $B > 134.77$; logical AND to form the combined mask; border exclusion (top/bottom text, left logo, right color bar); 3×3 neighbor cleanup ($\geq$4 neighbors). A sliding square window (∼5% of the larger side, clamped for scale) produces a density map; the peak locates the most concentrated set of 1s in the mask. The first row of `thermography_2.png` presents the original image, the combined mask, and the hotspot visualization with the high-contrast square. The second row presents the thresholded Green, Red, and Blue channels. All images are rendered at high resolution (600 dpi) to preserve measurement detail.

Figure 3 shows, in the upper row, the original thermographic image, the combined mask obtained after thresholding, and the hotspot identification overlaid on the original image. In the lower row, the figure presents the decomposed color-channel images (Green, Red, and Blue), after applying the corresponding thresholding step.

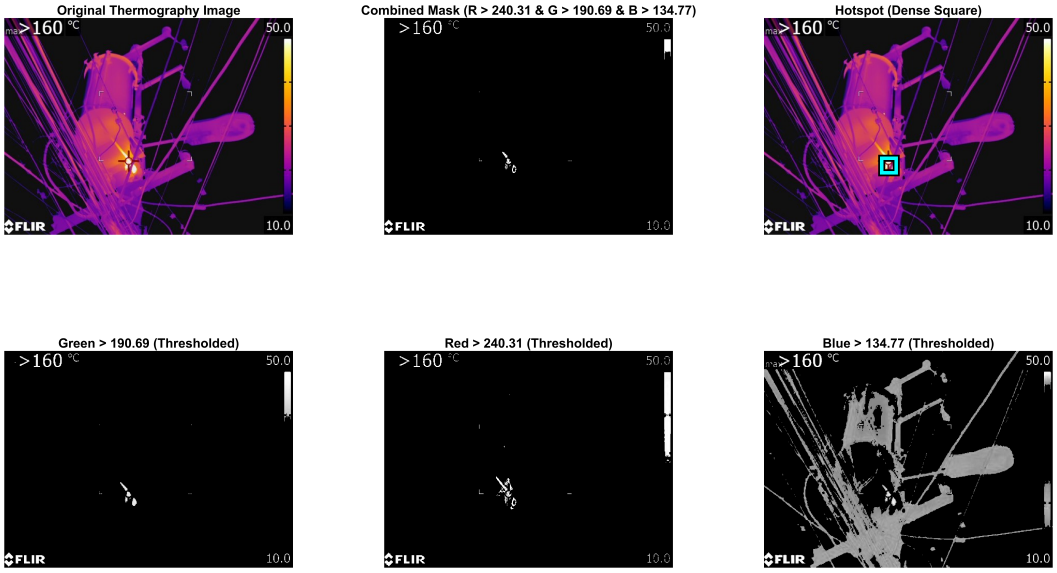

Figure 3. Image processing in the Matlab program of case 2.

Table 8 reports the matrix-structure parameters of the thermographic image used in Case 2 and its derived arrays. These parameters document the data structure of the processed image and support reproducibility of the pipeline.

As a result of the thermographic image through image processing, the following coordinates were obtained in [X Y] [329–334 : 238–242], which will allow finding the hot spot, obtaining precise data, and the exact location of the transformer fault, as shown in Table 9.

Table 8. Dimensioning of the matrix generated by the thermographic matrix case 2.

Name	Value
a	423 × 563 × 3 uint8
ab	423 × 563 uint8
ag	423 × 563 uint8
ar	423 × 563 uint8
ca	563
fa	423
i	423
ii	563
pcg	419 × 558 uint8
pcr	413 × 559 uint8

Table 9. Hot spot location at coordinates [X Y] [244 334].

pcr	pcg	ca	ar	a				
419 × 558 uint8				**Matrix Sizing**				
		238	239	240	241	242	243	244
329	0	255	254	0	0	255	0	0
330	0	255	252	0	0	255	0	0
331	0	255	0	0	0	255	0	0
332	0	255	254	0	0	255	0	0
333	0	255	252	0	0	255	0	0
334	0	255	252	253	0	255	0	0

Finally, Tables 10 and 11 presents the results obtained using the image-processing technique. Finally, it presents evidence from the study, analyzing faults in the transformers at the primary A-04 Chimbacalle substation.

Table 10. Transformer diagnostics (part 1).

Transformer	Location	Coordinates	Failure Detected	Algorithm Detected
1	Eduardo Bata y Guayllabamba	−0.240531, −78.510462	Yes	Yes
2	Abel Meléndez y Napo	−0.241486, −78.512429	Yes	Yes
3	E7B Y Francisco Olmos	−0.247627, −78.503040	Yes	Yes
4	Alonso Lobon y Sucumbíos	−0.243715, −78.506570	Yes	Yes
5	Alpahuasi Y Borgoñon	−0.243211, −78.512102	Yes	Yes
6	Benjamin Lastra y Primero de Mayo	−0.245985, −78.515103	Yes	Yes
7	Pedro Cepero y Alpahuasi	−0.245214, −78.510506	Yes	Yes

Overview. The results draw from a field dataset of over 500 thermograms acquired on distribution assets and reported with full radiometric context (camera settings, emissivity,

distance, shaded T_{ref}). Apparent readings are converted to surface temperature, and ΔT is computed against a shaded reference ROI. Hotspot masks are obtained with an adaptive pipeline (per-image Otsu threshold with a percentile fallback and chromatic guards), yielding consistent ROIs and statistics (max/mean). To make performance transparent, the section juxtaposes fault-positive cases—where elevated ΔT and contact locations indicate degradation—with fault-negative cases under comparable ambient/load conditions where the method rightly refrains from flagging faults.

Table 11. Transformer diagnostics (part 2).

Hot Spot Coordinates	RGB Coordinates	Start Coordinates (X,Y)	End Coordinates (X,Y)	Detected (This Sample)
[X Y] [90 60]	[254 230 204]	(88, 58)	(88, 64)	Yes
[X Y] [244 334]	[111 22 16]	(239, 237)	(247, 354)	Yes
[X Y] [316 134]	[230 234 160]	(255, 85)	(295, 200)	Yes
[X Y] [185 143]	[233 229 243]	(187, 141)	(183, 169)	Yes
[X Y] [391 249]	[235 242 235]	(387, 245)	(388, 281)	Yes
[X Y] [285 365]	[232 235 122]	(283, 358)	(285, 368)	Yes
[X Y] [194 101]	[232 107 43]	(212, 29)	(185, 244)	Yes

6. Discussion: Model-Based Interpretation and Implications for Corrosion and Materials Degradation

Relationships based on mixed potential, Stern–Geary, and Randles circuits assume specific interface behaviors. This study operates within ranges where linearizations are valid: moderate overpotentials, currents within the linear EIS regime, and temperatures close to those for which parameterizations were obtained. Deviations (e.g., severe polarization, surface films, or pollutant loads outside calibration) can bias estimates of i_{corr} and R_p; when such conditions are suspected, the analysis refrains from numerical inference and recommends direct electrochemical characterization.

This study hypothesizes (and prior literature suggests) that tightening under mechanical degradation reduces R_{eff}. To validate this, this study defines an experimental sequence: (i) baseline thermogram and DC resistance/EIS; (ii) torque procedure with calibrated wrench and tolerance logging; (iii) immediate post-torque DC/EIS; (iv) 24–72 h follow-up. The evolution of R_{eff} and ΔT across these steps will be reported with measurement tolerances. This was not executed in the current dataset and is listed as a limitation.

The concentrated model of Equation (10) applies to connectors in which heat generation is dominated by localized contact resistance and the accessible surfaces are radiometrically observable: bolted/clamped lugs, compression terminals, bus joints, and bushing terminals with minimal shrouding. Extension to geometries with distributed heating (e.g., long cable runs, encapsulated joints) or strong internal convection requires either a refined thermal network or FEM calibration.

Generalizability to Different Environments and Equipment Types

The method is designed to be transferable, but its decision quality depends on acquisition conditions and the infrared camera's temperature rendering. First, different climates (humidity, pollution, salt deposition, and diurnal temperature swings) modify both corrosion kinetics and thermographic confounders (time of wetness, solar loading, and wind cooling). Consequently, the same ΔT threshold can correspond to different degradation stages unless emissivity, reflected temperature, and operating current are controlled or uncertainty-bounded (Equations (13) and (16)). Second, different equipment types (trans-

former bushings, bolted bus joints, compression lugs, clamps, and switchgear contacts) present different heat-sink paths and therefore different θ_{th}; a calibration (step-current thermography or FEM) is required before comparing R_{eff} across geometries. Third, the RGB decomposition step is camera- and palette-dependent: pseudo-color exporters may map temperature to RGB using different colormaps, making fixed RGB thresholds non-universal. For this reason, the manuscript treats RGB-channel thresholding as a surrogate to be used only when radiometric temperature fields are unavailable, and it recommends validating the thresholds per camera/export mode using the performance metrics in Section 4.

To strengthen sensitivity reporting beyond ideal emissivity and capture-distance conditions, the workflow includes (i) repeated captures at two distances within the safe operating window, (ii) a bracket on emissivity (e.g., $\varepsilon \pm 0.05$ for oxidized metal) to bound temperature bias, and (iii) a "confounder-present" rule that triggers rescan or conservative reclassification (Table 5). These steps explicitly target generalization across typical field variability.

This study's approach complements recent hybrid FEM–AI and sensor–AI monitoring work by explicitly exposing the physics-to-image pathway and the measurement assumptions. This study differs in (i) focusing on radiometric transparency (documented camera settings, emissivity, and corrections), and (ii) prioritizing uncertainty and sensitivity reporting before model scoring. This positioning helps bridge thermographic diagnostics with reproducible, bias-aware hybrid models.

This study revisits Holm's contact theory, corrosion kinetics, and reliability models to interpret observed hotspots. Where concrete data exist (single-visit thermograms and ROI statistics), this study anchors the discussion to the reported ΔT and corrected temperatures. Elements that require repeated measurements or dedicated instrumentation (e.g., EIS for R_{eff}, retorquing-and-reinspection studies, or Weibull fits across a fleet) are explicitly framed as future work, not as validated components of the present dataset.

The mathematical framework in Section 2 explains the empirical thermograms by explicitly linking contact degradation and corrosion kinetics to temperature rise. First, Equations (8)–(10) indicate that small increases in R_{eff} (due to oxide films or loss of clamping force) produce quadratic increases in dissipated power with the operating current. Second, EIS-derived R_{ct} values feed Equation (2) to estimate i_{corr}, which in turn allows computing thickness-loss rates via Equation (4). Third, the Arrhenius form (5) rationalizes the observation that assets in warmer microclimates or subject to solar loading deteriorate faster. Finally, uncertainty budget Equations (13)–(17) identify the parameters that must be controlled in field surveys (e.g., emissivity and reflected temperature) to maintain decision-grade accuracy.

Case Interpretation: For the reported case studies (Sections on Substation A-04 Chimbacalle and Abel Meléndez), the measured hot spots can be translated into estimates of R_{eff} using Equation (10) once θ_{th} is characterized (by simple step-current tests or finite-volume thermal models). Combining R_{eff} trends with periodic EIS or DC resistance measurements allows separation of purely mechanical looseness from chemically driven film growth. If R_{eff} decreases after retorquing, mechanical causes dominate; if not, corrosion/contamination is likely predominant, and cleaning and surface protection are warranted.

Risk and Maintenance Prioritization: The Weibull–Arrhenius model (Equation (18)) produces a probability-of-failure forecast conditioned on the observed ΔT. Assets with high ΔT (hence low η) should be scheduled for immediate maintenance; those with moderate ΔT qualify for closer monitoring and cleaning; assets with low ΔT can remain on routine inspection cycles. This quantitative triage exceeds qualitative color-thresholding alone and is aligned with reliability-centered maintenance practices [18].

This study hypothesizes—consistent with prior reports—that re-torquing mechanically degraded connectors reduces R_{eff}, but matched before- and after-electrical data are not available in the present field set. To validate this prospectively (without altering the journal template), the discussion frames a future protocol: (i) acquire a baseline thermogram with shaded T_{ref}, fixed emissivity and distance, and logged load I; (ii) measure four-wire DC resistance (resolution $\leq$1 mΩ) and, where clearance and safety permit, a short EIS sweep (e.g., 10 kHz–0.5 Hz) to estimate R_p; (iii) apply re-torque using a calibrated wrench at the manufacturer's nominal value (tolerance $\pm$4% full-scale), either in a single step or in 10% increments; (iv) allow 5–10 min thermal stabilization at comparable load/ambient; and (v) repeat DC/EIS and thermography under the same settings and again at 24–72 h. The evolution of ΔT, four-wire R_{eff}, and (when available) EIS-derived R_p will be reported with instrument tolerances and propagated uncertainty, providing a defensible before/after assessment of tightening effects; until then, this mechanism is treated as a limitation and a target for future validation.

7. Conclusions

This work is based on dozens of thermographic images collected in Quito, Ecuador. Two of the results are presented in detail, and Table 8 lists seven fault cases across different elements of the distribution system.

Beyond visual diagnostics, the present work establishes a predictive, physics-based bridge between corrosion/electrochemical metrics and thermographic evidence. The proposed parameter-estimation workflow enables objective trending of degradation, supports auditable maintenance decisions, and facilitates reproducibility. Future work may integrate Bayesian filtering for online updating and couple EIS-thermal data with mechanistic models of film growth under cyclic loading and pollution deposition.

The developed method facilitates fault localization at any voltage level by detecting a temperature rise, commonly referred to as a hot spot. According to Joule's law, it speaks about an abnormal growth of ohmic resistance; that is why thermography based on image processing allows us to calculate, check and visualize without contact and at a long distance the temperatures of a surface with accuracy in electrical power systems without putting out of service distribution and switching systems. This helps to produce accurate thermographic reports that clearly specify the location and type of fault or hot spot found by means of a digital and an infrared image, which saves maintenance time.

Author Contributions: Conceptualization, M.R. and C.B.; methodology, M.R.; software, C.B.; validation, M.R. and C.B.; formal analysis, C.B.; investigation, C.B.; resources, C.B.; data curation, M.R.; writing—original draft preparation, M.R. and C.B.; writing—review and editing, M.R.; visualization, M.R.; supervision, M.R.; project administration, M.R.; funding acquisition, M.R. All authors have read and agreed to the published version of the manuscript.

Funding: This research received no external funding and was supported by Universidad Politécnica Salesiana.

Institutional Review Board Statement: Not applicable.

Informed Consent Statement: Not applicable.

Data Availability Statement: The original contributions presented in this study are included in the article. Further inquiries can be directed to the corresponding author.

Conflicts of Interest: The authors declare no conflicts of interest.

Nomenclature

i, i_0, i_{corr}	net, exchange, and corrosion current densities ($A\,m^{-2}$)
η	overpotential (V)
β_a and β_c	Tafel slopes (V/dec)
R_p	polarization resistance ($\Omega\,m^2$)
R_{ct}, R_s	charge transfer and solution/film resistances ($\Omega\,m^2$)
Y_0, n	CPE magnitude ($S\,s^n\,m^{-2}$) and exponent (−)
E_a	activation energy ($J\,mol^{-1}$)
R	gas constant ($J\,mol^{-1}\,K^{-1}$)
F	Faraday constant ($C\,mol^{-1}$)
ρ_m, ρ_f, δ	metal and film resistivities ($\Omega\,m$) and film thickness (m)
I	electrical current (A)
R_{eff}	effective contact resistance (Ω)
θ_{th}	thermal resistance ($K\,W^{-1}$)
A_{ext}	external area (m^2)
ε, τ	emissivity (−) and atmospheric transmittance (−)
ΔT	steady-state temperature rise (K)
T_∞	ambient temperature (K)

References

1. Alotaibi, M.; Shakibaei Asli, B.H.; Khan, M. Non-Invasive Inspections: A Review on Methods and Tools. *Sensors* **2021**, *21*, 8474. [CrossRef] [PubMed]
2. Cheng, L.; Zhu, Y.; Kersemans, M. DMD-T: Thermographic Inspection of Composites Using Dynamic Mode Decomposition. In Proceedings of the 5th International Conference on Industrial Artificial Intelligence (IAI), Shenyang, China, 21–24 August 2023; pp. 1–4. [CrossRef]
3. Usamentiaga, R.; Venegas, P.; Guerediaga, J.; Vega, L.; Molleda, J.; Bulnes, F. Infrared Thermography for Temperature Measurement and Non-Destructive Testing. *Sensors* **2014**, *14*, 12305–12348. [CrossRef] [PubMed]
4. *ISO 9223:2012*; Corrosion of Metals and Alloys: Corrosivity of Atmospheres—Classification, Determination and Estimation. ISO: Geneva, Switzerland, 2012.
5. Pratticò, D.; De Carlo, D.; Silipo, G.; Laganà, F. Hybrid FEM-AI Approach for Thermographic Monitoring of Biomedical Electronic Devices. *Computers* **2025**, *14*, 344. [CrossRef]
6. Tzvetkova, S.; Lozanov, Y.; Petleshkov, A. Thermographic assessment of the technical condition of photovoltaic power plants—A case study. In Proceedings of the 2024 16th Electrical Engineering Faculty Conference (BulEF), Sofia, Bulgaria, 19–22 September 2024; pp. 1–4. [CrossRef]
7. Verma, C.; Aslam, J.; Aslam, R.; Zehra, S.; Hussain, C.M. *Handbook of Corrosion Engineering: Modern Theory, Fundamentals and Practical Applications*; Elsevier: Amsterdam, The Netherlands, 2023. [CrossRef]
8. Vollmer, M.; Möllmann, K.-P. *Infrared Thermal Imaging: Fundamentals, Research and Applications*, 2nd ed.; Wiley-VCH: Weinheim, Germany, 2018; ISBN 9783527413515.
9. Becker, J.; Diler, E.; Tanguy, F.; Vucko, F. Machine Learning-Based Corrosion Rate Prediction for Zinc and Steel Using Real-Time Corrosion Sensors in Accelerated Corrosion Test Conditions. In Proceedings of the 2025 International Conference on Emerging Technologies and Computing (IC_ETC), Brest, France, 23–26 June 2025; pp. 1–5. [CrossRef]
10. López-Pérez, S.; Antonino-Daviu, J.A. Application of Infrared Thermography to Failure Detection in Industrial Induction Motors: Case Stories. *IEEE Trans. Ind. Appl.* **2017**, *53*, 1901–1908. [CrossRef]
11. Guo, D.; Liu, Y.; Mei, H.; Tu, Y.; Wang, H. Nondestructive Evaluation of Composite Bonding Structure Used in Electrical Insulation Based on Active Infrared Thermography. *Polymers* **2022**, *14*, 3373. [CrossRef] [PubMed]
12. Hao, F.; Wang, S.; Ling, Y.; Zeng, Q. Infrared Thermal Measurement in Power System Considering Complex Circumstances. *J. Phys. Conf. Ser.* **2024**, *2876*, 012001. [CrossRef]
13. Hou, Y.; Zhang, X.; Zhou, Y. Review on Infrared Imaging Technology. *Sustainability* **2022**, *14*, 11161. [CrossRef]
14. Vavilov, V.; Burleigh, D. *Infrared Thermography and Thermal Nondestructive Testing*; Springer: Cham, Switzerland, 2020. [CrossRef]
15. Kaplan, H. *Practical Applications of Infrared Thermal Sensing and Imaging Equipment*, 3rd ed.; Tutorial Texts in Optical Engineering TT75; SPIE Press: Bellingham, WA, USA, 2007; ISBN 9780819467232.
16. *ISO 18434-1:2008*; Condition Monitoring and Diagnostics of Machines: Thermography—Part 1: General Procedures. ISO: Geneva, Switzerland, 2008.

17. Modest, M.F.; Mazumder, S. *Radiative Heat Transfer*, 4th ed.; Academic Press: London, UK, 2022; ISBN 9780323984065.
18. Li, Z.; Fu, H.; Guo, J. Reliability Assessment of a Series System with Weibull-Distributed Components Based on Zero-Failure Data. *Appl. Sci.* **2025**, *15*, 2869. [CrossRef]

Disclaimer/Publisher's Note: The statements, opinions and data contained in all publications are solely those of the individual author(s) and contributor(s) and not of MDPI and/or the editor(s). MDPI and/or the editor(s) disclaim responsibility for any injury to people or property resulting from any ideas, methods, instructions or products referred to in the content.